

Monodispersed Sulfur Nanoparticles for Lithium–Sulfur Batteries with Theoretical Performance

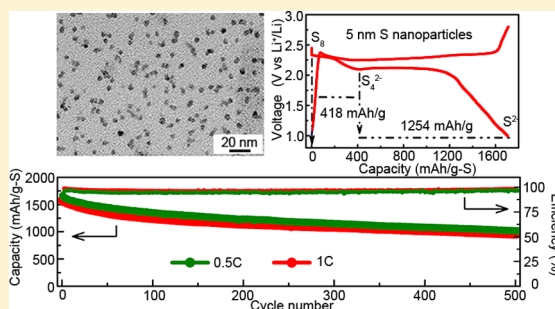
Hongwei Chen,[†] Changhong Wang,^{†,‡} Weiling Dong,[†] Wei Lu,[†] Zhaolong Du,^{†,‡} and Liwei Chen^{*,†}

[†]i-Lab, Suzhou Institute of Nano-Tech and Nano-Bionics (SINANO), Chinese Academy of Sciences, Suzhou 215123, China

[‡]Nano Science and Technology Institute, University of Science and Technology of China, Suzhou 215123, China

S Supporting Information

ABSTRACT: While Li–S batteries are poised to be the next generation high-density energy storage devices, low sulfur utilization and slow rate performance have limited their practical applications. Here, we report the synthesis of monodispersed S₈ nanoparticles (NPs) with different diameter and the nanosize dependent kinetic characteristics of the corresponding Li–S batteries. Most remarkably, 5 nm S NPs display the theoretical discharging/charging capacity of 1672 mAh g^{−1} at 0.1 C rate and a discharge capacity of 1089 mAh g^{−1} at 4 C.



KEYWORDS: Sulfur nanoparticle, theoretical specific capacity, Li–S battery, nanosize effect

Sulfur is a promising cathode material with a high theoretical specific capacity of 1672 mAh g^{−1}. When paired with lithium metal anode to form rechargeable lithium–sulfur (Li–S) batteries, the theoretical specific energy density can be as high as 2600 Wh kg^{−1}.¹ These estimations have inspired high expectations in meeting future large-scale energy storage needs; however, low sulfur utilization, short cycle life, and low Coulombic efficiency have hindered practical application of Li–S batteries.^{2,3}

A major bottleneck is the slow charge transfer kinetics resulting from poor electronic conductivity of sulfur and the final discharge product, Li₂S. Similar challenges were encountered in LiFePO₄-based cathode materials of lithium ion battery and are successfully overcome via preparation of nanosized particles with conductive carbon coating.^{4,5} The lithium sulfur battery field has made remarkable progresses via a related approach, that is, by using nanostructured carbon–sulfur composite cathode materials, which typically consist of sulfur active material infiltrated in nanoporous conducting carbon frameworks. However, unlike the intercalation/deintercalation process in LiFePO₄, the Li–S system is based on complicated multistep redox reactions between lithium and sulfur involving a solid–solution–solid transition. The influence of materials size in such a complicated battery system has not been investigated and thoroughly understood.

As illustrated in Figure 1a, the multistep discharging process of Li–S batteries can be divided into three stages: (I) solid-to-solution reduction of S₈ to long chain polysulfides; (II) solution phase reduction of long chain polysulfides to short-chain polysulfides; and (III) solution-to-solid reduction of short-chain polysulfides to insoluble and insulating Li₂S₂ and Li₂S. In galvanostatic discharging curves, the three stages correspond to

the high and low voltage plateaus and the tailing slope with increasing over potential toward the end of discharge. Theoretical discharge behavior predicts a total capacity of 1672 mAh g^{−1} with stages I, II, and III displaying 25% (stage I) and 75% (stage II and III) of total capacity, respectively. However, such theoretical behavior has not been experimentally realized. Figure 1b–f hypothetically illustrates multiple microscopic scenarios. For example, dissolution of S₈ in stage I may cause the loss of electrical contact for part of unreacted sulfur (Figure 1b); unrestricted diffusion of polysulfides in electrolyte results in their reaction with anode Li metal (Figure 1c), thus partially losing the capacity in stage II; in stage III, the insulating nature of reduction product Li₂S may block further reduction of polysulfides (Figure 1d). Furthermore, kinetic factors may also affect the battery performance: a large flux of Li⁺ migrate to the surface of S particle under high discharging rate, which leads to fast formation of a Li₂S layer, which may block the diffusion of Li⁺ toward the interior of the particle (Figure 1e); and similarly, high rate discharge may also result in the formation of Li₂S layer on Li₂S₂ (in stage III) and hence incomplete reduction of Li₂S₂ (Figure 1f).

Because these processes can be profoundly affected by the size of sulfur materials, we hypothesize that there exists nanosize effect in Li–S batteries, that is, the size of sulfur particles may significantly impact the discharging behavior. On the basis of the analysis above, small sulfur particle size may lead to better sulfur utilization, and the larger specific surface area leads to smaller effective current density and enables faster discharging kinetics. The trade-off between high specific

Received: December 24, 2014

Published: December 29, 2014

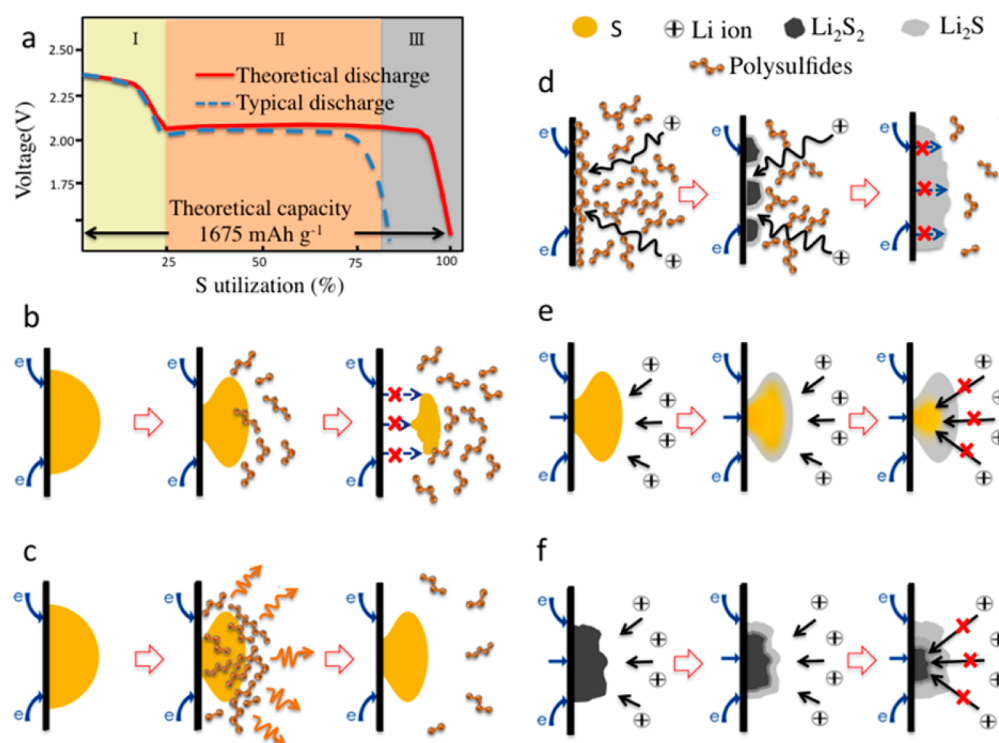


Figure 1. Schematic illustrations of the nanosize effect in Li-S cathodes. (a) Theoretical and typical experimental discharge curves of S₈-based cathodes. (b) Dissolution of S₈ in discharge stage I, loss of electrical contact with electrode in large S particles causes incomplete utilization of S; (c) diffusion of polysulfides in discharge stage I and II; (d) reduction of polysulfides to Li₂S₂ and Li₂S, large particle size may block the electron transfer; (e) large flux of Li⁺ forms a Li₂S blocking layer on S particle surface although this effect is less severe in small particles due to large specific surface area; and (f) formation of Li₂S blocking layer on Li₂S₂ surface, similar to the process in (e).

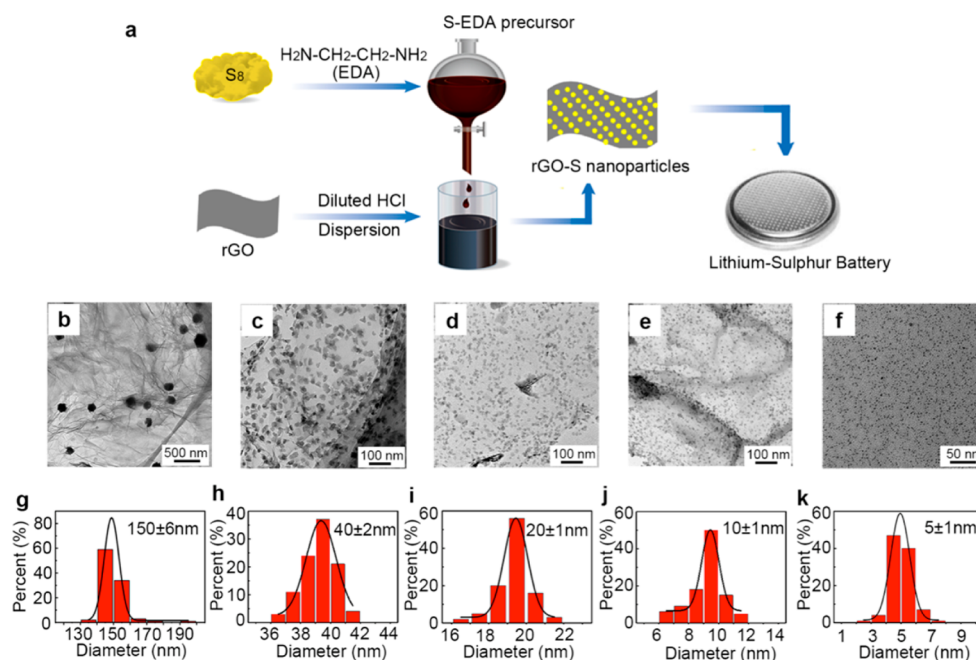


Figure 2. Synthesis of monodispersed S nanoparticles. (a) Schematic illustration of the synthetic procedure. Sulfur nanoparticles (S NPs) of varying size are deposited on rGO surface via the sulfur-amine chemistry. The reaction parameters for different S NP size are listed in the Supporting Information Table S1. TEM micrographs showing (b) 150 nm S NPs, (c) 40 nm S NPs, (d) 20 nm S NPs, (e) 10 nm S NPs, and (f) 5 nm S nanoparticles deposited on rGO. The scale bars in (b), (c–e), and (f) are 500, 100, and 50 nm, respectively. Histograms of S NP size distribution obtained from analyses of 100–200 particles for each size from the TEM images: (g) 150, (h) 40, (i) 20, (j) 10, and (k) 5 nm S NPs.

capacity and high rate performance may thus be resolved in ultrasmall sulfur nanoparticles.

In this study, we synthesize a series of monodispersed S nanoparticles with different diameter and demonstrate that the electrochemical performance is critically dependent on the

sulfur particle size. The results confirm the nanosize effect in Li–S batteries. Importantly, we demonstrate that the theoretical discharging behavior can be experimentally realized in ultrasmall sulfur nanoparticles.

We first prepared a series of monodispersed S NPs with different diameter on reduced graphene oxide (rGO) via the sulfur-amine chemistry (Figure 2a).⁶ The sulfur-ethylenediamine complex precursor is dropwise added to rGO dispersion in water/ethanol mixed solvents. The sulfur-amine complex decomposes to release elemental sulfur, and octaatomic S₈ particles nucleate on the surface of rGO sheets. By carefully adjusting reaction conditions such as deposition time and solution pH, monodispersed S NPs with their diameter ranging from 150, 40, 20, 10 to 5 nm are prepared (Supporting Information Table S1).

Figure 2b–f presents transmission electron microscopy (TEM) micrographs of S NPs homogeneously loaded on rGO surfaces without aggregation. Particle size analysis histograms show that the diameter distributions are fairly narrow (Figure 2g–k). More TEM images of these S NPs with different magnifications are available in Supporting Information Figures S1–S3. Energy-dispersive X-ray spectroscopy (EDX) mapping of carbon and sulfur in the 5 nm S NP sample further confirms the uniform distribution of S element on rGO surface (Supporting Information Figure S4).

The narrow size distribution of the S NPs is corroborated by ensemble measurements. Thermogravimetric (TG) analysis in Figure 3a shows steep weight loss curves and the sublimation temperature shifts toward lower temperature as the size of S NPs decreases. The downshift of the sublimation temperature is mainly due to excess surface free energy of small S NPs as well as the larger contact area between smaller S NPs and rGO, which facilitates the heat transfer.^{7,8} The TG analysis also

shows that the S loading in these rGO–S NPs composites are all 80%, except for that of the smallest 5 nm S NPs, which is 70%. Figure 3b shows the powder X-ray diffraction (XRD) of the S NPs. The samples exhibit the characteristic diffraction peaks of orthorhombic S₈,^{9,10} except for the smallest sized 5 nm S NPs, which is featureless in XRD, indicating its close-to-amorphous structure due to small particle size. Supporting Information Table S2 displays the full width at half-maximum (fwhm) of the main diffraction peak at 23.06°. The diffraction peak consistently broadens as the particle size reduces. These data confirm that the particle size is well controlled, which lays a solid basis for the following discussion on size-dependent battery performances.

The rGO–S NPs composites are assembled in CR-2025 coin-type cells as the cathode material and their electrochemical performances are examined. Figure 4a presents the initial galvanostatic discharge/charge profiles under 0.25 C (1 C = 1672 mA g^{−1}). All discharging curves show the high-potential plateau at ~2.3 V and the low-potential plateau (~2.1 V) with a tailing slope, which are consistent with the solid–liquid–solid transformation illustrated in Figure 1a.^{3,11} Smaller-sized S NPs exhibit greater overall specific capacity as well as greater capacity in discharge plateaus, suggesting better utilization of sulfur in smaller NPs. Moreover, as shown in Figure 4b, the EIS spectra of all S NPs show a depressed semicircle in the high frequency region followed by an inclined line in the low frequency region. The charge transfer resistance, R_{ct} , obtained from the fitting results exhibit a significant and monotonic decrease as the diameter of S NP decreases, indicating faster kinetics in smaller S NPs (see Supporting Information Figure S5).^{12,13} Because the R_{ct} of as-prepared batteries mainly reflects the resistance of the electrode/electrolyte interface, the decrease of R_{ct} with decreasing S NP size can be attributed to large specific surface area and improved electrical contact between the conducting agent and small S NPs.

Figure 4c shows the cycling performance at 0.25 C. These batteries show good cycle stability, keeping 70–80% of the initial capacity after 100 cycles. Both the capacity retention ratio and Coulombic efficiency improve steadily as the S NP size reduces (Supporting Information Table S3). The improved cycling stability probably originates from restricted polysulfide diffusion due to increased specific contact area with rGO in smaller S NPs. Graphene-based materials have demonstrated strong sulfur adsorption effects derived from the high specific surface area.¹⁴ In addition, residual functional groups on rGO surface may also contribute to the immobilization of sulfur or polysulfides. Both effects help to alleviate the shuttle effect and improve the cycle stability.¹⁴

Figure 4d shows the rate performance of these batteries. At current density of 4 C, the specific capacities are 231, 442, 689, 886, and 1089 mAh g^{−1} for 150, 40, 20, 10, and 5 nm S NPs, respectively. Particularly, the rate performance of the 5 nm S NP cell has exceeded all previous reports based on the cyclic octaatomic S₈ material.^{15–20} The galvanostatic discharge/charge profiles of S NPs at different rates are presented in Supporting Information Figure S6. The capacity of the high-potential plateau decreases with increased rate for 150 and 40 nm S NPs but remains nearly constant for 20, 10, and 5 nm S NPs (indicated with the solid black arrows in Supporting Information Figure S6). Small S particle size facilitates electron and Li⁺ diffusion and leads to better S utilization and higher specific capacity. In addition, large specific surface area of small S particles effectively reduces discharging current density and

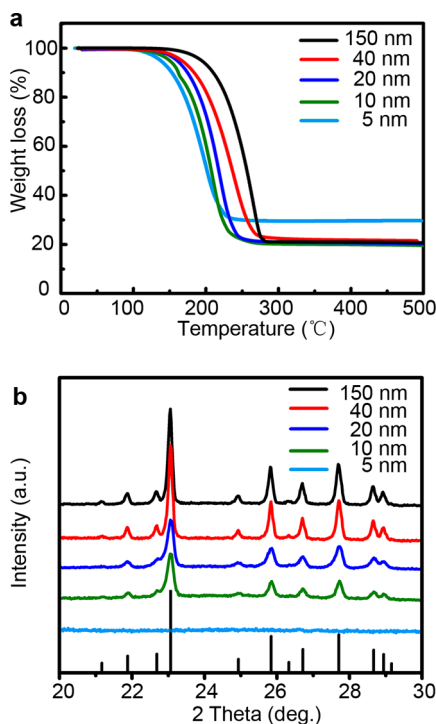


Figure 3. (a) Thermogravimetric and (b) X-ray diffraction analyses of S NPs; standard XRD pattern of orthorhombic S₈ is marked at the abscissa.

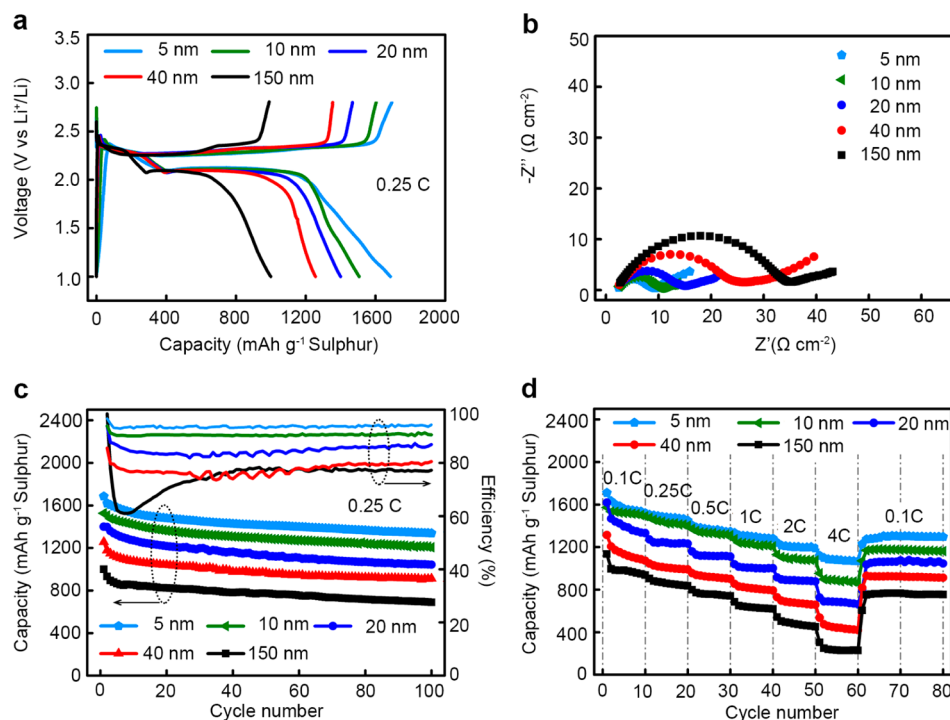


Figure 4. Electrochemical performance of S NPs in Li-S batteries. (a) Initial galvanostatic discharge/charge profiles under 0.25 C, (b) electrochemical impedance spectra of as-prepared batteries, (c) cycling performance and Coulombic efficiency under 0.25 C, (d) rate performance at current density from 0.1 to 4 C.

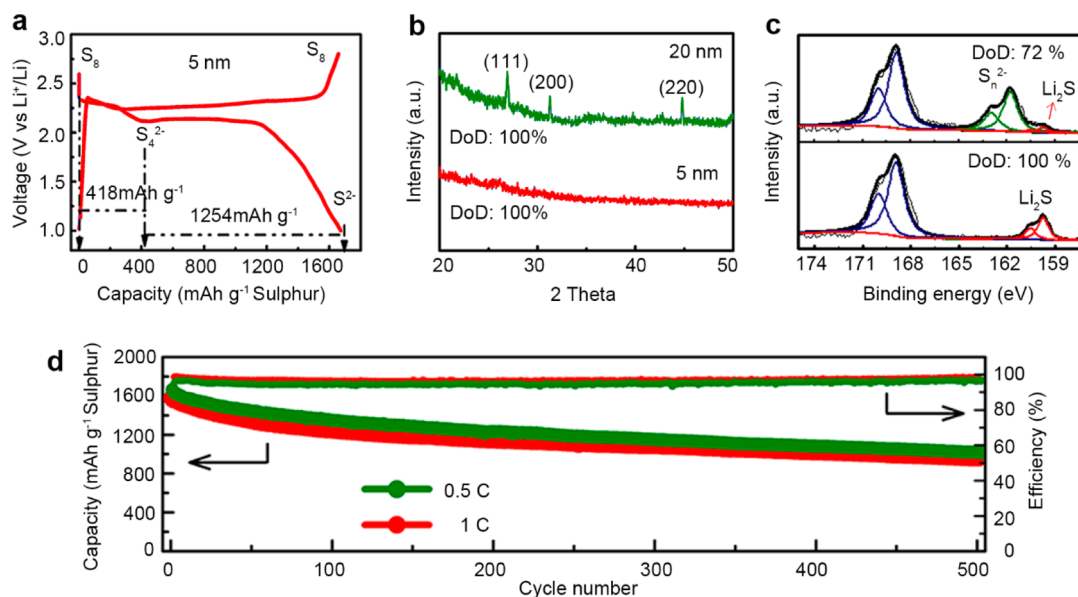


Figure 5. Theoretical discharging behavior and high cycle stability of the 5 nm S NP. (a) Experimental discharge/charge profile of 5 nm S NPs at 0.1 C. (b) XRD patterns of the discharge products of 20 and 5 nm S NPs discharged to 1.0 V (at DoD of 100%), respectively. (c) XPS spectra of discharge products of 5 nm S NPs at DoD of 72 and 100%. (d) Cycling performance of 5 nm SNPs at current density of 0.5 C and 1 C.

Li⁺ flux and thus may alleviate the formation of Li₂S blocking layer in high rate discharge.

Nanosized sulfur facilitates the charge transfer process and enhances the utilization of sulfur. Detailed characterization of the 5 nm S NPs reveals that the ultrasmall S NP exhibits theoretical behavior of the sulfur cathode material. Figure 5a shows the initial discharge/charge profile of the 5 nm S NPs, whose specific capacity reaches 1672 mAh g⁻¹ at the current density of 0.1 C (the capacity of rGO, 35 mAh g⁻¹, has been

subtracted, Supporting Information Figure S7). The discharge profile matches very well with theoretical prediction.²¹ The high-potential plateau at about 2.35 V exhibits capacity of 418 mAh g⁻¹, and the low-potential plateau at about 2.14 V together with the subsequent tailing slope exhibit capacity of 1254 mAh g⁻¹.²¹ When using XRD to test the discharged products of 5 nm S NP and 20 nm S NP, compared to 20 S NP, 5 nm S NP does not display any peaks (see in Figure 5b).^{22,23} So X-ray photoelectron spectra (XPS) was utilized to

characterize 5 nm S NP at different depth of discharge (DoD). Figure 5c at the DoD of 72% shows two peaks at binding energy of 161.8 and 162.9 eV that are assigned to S_n^{2-} ($2 \leq n \leq 4$),^{24,25} while at DoD of 100% the peaks shift to lower binding energy of 159.8 and 160.8 eV,²⁰ which are characteristic to Li_2S . These results indicate that Li_2S is the only major product after discharged to 1.0 V and that octaatomic S_8 can indeed be completely utilized in the form of ultrasmall S NPs.

Figure 5d displays the cycling performance of the 5 nm S NP at 0.5 C and 1 C. When cycled at 0.5 C, the specific capacity is 1661 mAh g⁻¹ at the first discharge and 1017 mAh g⁻¹ after 500 cycles, with Coulombic efficiency stabilized at 96%. When cycled at 1 C, the specific capacity is 1574 mAh g⁻¹ at the first discharge and 965 mAh g⁻¹ after 500 cycles, with Coulombic efficiency stabilized at 98%. The capacity decay rate is as low as 0.077%. Long-term cycle stability further demonstrates the suppression of polysulfide diffusion due to stronger absorption and large contact area between small S NPs and rGO.

Octaatomic S_8 is the most commonly available form of elemental sulfur; therefore, understanding the limiting factors in reaching the theoretical performance of S_8 is highly important for the Li–S battery technology. Our results confirmed that the theoretical limit of specific capacity and the theoretical discharge/charge behavior of Li–S battery can indeed be achieved when the S particle size reduced down to ultrasmall 5 nm.

In summary, monodispersed sulfur NPs with the diameter ranging from 150 to 5 nm were uniformly deposited on rGO surface via the sulfur-amine chemistry. The S NPs exhibit higher specific capacity and better rate performance in Li–S batteries with decreased particle size. Large S particle size and high discharging rate kinetically result in high Li^+ concentration at sulfur particle surface and thus form an insulating Li_2S_2 and Li_2S blocking layer. Small sulfur particle size and low discharging rate allow for Li^+ diffusion into the interior of sulfur particle, thus delaying the formation of the insulating Li_2S_2 and Li_2S and improving the sulfur utilization. When sulfur particle size is down to 5 nm, the specific capacity reaches the theoretical specific capacity of 1672 mAh g⁻¹ at 0.1 C, and 1089 mAh g⁻¹ even at 4 C, and the specific capacity remains at 1017 and 965 mAh g⁻¹ after 500 cycles at 0.5 C and 1 C, respectively. These results indicate that the charge transfer and mass transport in Li–S cathode is a kinetic process highly dependent on the particle size and discharge/charge rate. Reducing the size of sulfur particles down to a few nanometers can greatly improve the utilization of sulfur and enhance the cycle stability and rate performance of Li–S batteries.

■ ASSOCIATED CONTENT

■ Supporting Information

Experimental procedures and additional physical/electrochemical characterization, including TEM, EDS, fwhm of XRD characteristic peak, EIS, profiles of rate capability, and capacity of pure rGO. This material is available free of charge via the Internet at <http://pubs.acs.org>.

■ AUTHOR INFORMATION

Corresponding Author

*E-mail: lwchen2008@sinano.ac.cn.

Author Contributions

H.C. and C.W. contributed equally to this work.

Notes

The authors declare no competing financial interest.

■ ACKNOWLEDGMENTS

This work was supported by the “Strategic Priority Research Program” of the CAS (Grant XDA09010600), the National Natural Science Foundation of China (Grants 21103222 and 21273273), and Science and Technology Projects of Suzhou (ZXJ2012002). W.L. thanks the Foundation of Creative Young Scientists, CAS. L.C. acknowledges the support from Jiangsu Provincial Natural Science Foundation (Grant BK201300006).

■ REFERENCES

- (1) Bruce, P. G.; Freunberger, S. A.; Hardwick, L. J.; Tarascon, J.-M. *Nat. Mater.* **2012**, *11* (1), 19–29.
- (2) Manthiram, A.; Fu, Y.; Su, Y.-S. *Acc. Chem. Soc.* **2012**, *46* (5), 1125–1134.
- (3) Zhang, S. S. *J. Power Sources* **2013**, *231*, 153–162.
- (4) Wang, J.; Sun, X. *Energy Environ. Sci.* **2012**, *5* (1), 5163–5185.
- (5) Sun, C.; Rajasekhara, S.; Goodenough, J. B.; Zhou, F. *J. Am. Chem. Soc.* **2011**, *133* (7), 2132–2135.
- (6) Wang, C.; Chen, H.; Dong, W.; Ge, J.; Lu, W.; Wu, X.; Guo, L.; Chen, L. *Chem. Commun.* **2014**, *50* (10), 1202–1204.
- (7) Guo, Y. G.; Hu, J. S.; Wan, L. J. *Adv. Mater.* **2008**, *20* (15), 2878–2887.
- (8) Wang, C.; Wan, W.; Chen, J.-T.; Zhou, H.-H.; Zhang, X.-X.; Yuan, L.-X.; Huang, Y.-H. *J. Mater. Chem. A* **2013**, *1* (5), 1716–1723.
- (9) Guo, J.; Xu, Y.; Wang, C. *Nano Lett.* **2011**, *11* (10), 4288–4294.
- (10) Zhang, K.; Zhao, Q.; Tao, Z.; Chen, J. *Nano Res.* **2013**, *6* (1), 38–46.
- (11) Zhang, S. S.; Tran, D. T. *J. Power Sources* **2012**, *211*, 169–172.
- (12) Li, W.; Zhang, Q.; Zheng, G.; Seh, Z. W.; Yao, H.; Cui, Y. *Nano Lett.* **2013**, *13* (11), 5534–5540.
- (13) Deng, Z.; Zhang, Z.; Lai, Y.; Liu, J.; Li, J.; Liu, Y. *J. Electrochem. Soc.* **2013**, *160* (4), A553–A558.
- (14) Ji, L.; Rao, M.; Zheng, H.; Zhang, L.; Li, Y.; Duan, W.; Guo, J.; Cairns, E. J.; Zhang, Y. *J. Am. Chem. Soc.* **2011**, *133* (46), 18522–18525.
- (15) Sun, H.; Xu, G.-L.; Xu, Y.-F.; Sun, S.-G.; Zhang, X.; Qiu, Y.; Yang, S. *Nano Res.* **2012**, *5* (10), 726–738.
- (16) Chen, R.; Zhao, T.; Lu, J.; Wu, F.; Li, L.; Chen, J.; Tan, G.; Ye, Y.; Amine, K. *Nano Lett.* **2013**, *13* (10), 4642–4649.
- (17) Lu, S.; Cheng, Y.; Wu, X.; Liu, J. *Nano Lett.* **2013**, *13* (6), 2485–2489.
- (18) Wang, H.; Yang, Y.; Liang, Y.; Robinson, J. T.; Li, Y.; Jackson, A.; Cui, Y.; Dai, H. *Nano Lett.* **2011**, *11* (7), 2644–2647.
- (19) Ji, L.; Rao, M.; Aloni, S.; Wang, L.; Cairns, E. J.; Zhang, Y. *Energy Environ. Sci.* **2011**, *4* (12), 5053–5059.
- (20) Lin, T.; Tang, Y.; Wang, Y.; Bi, H.; Liu, Z.; Huang, F.; Xie, X.; Jiang, M. *Energy Environ. Sci.* **2013**, *6* (4), 1283–1290.
- (21) Barchasz, C. I.; Molton, F.; Duboc, C.; Leprêtre, J.-C.; Patoux, S. b.; Alloin, F. *Anal. Chem.* **2012**, *84* (9), 3973–3980.
- (22) Mizuno, F.; Hayashi, A.; Tadanaga, K.; Tatsumisago, M. *Adv. Mater.* **2005**, *17* (7), 918–921.
- (23) Eckert, H.; Zhang, Z.; Kennedy, J. H. *Chem. Mater.* **1990**, *2* (3), 273–279.
- (24) Su, Y.-S.; Fu, Y.; Cochell, T.; Manthiram, A. *Nat. Commun.* **2013**, *4*, 2985–2992.
- (25) Fu, Y.; Zu, C.; Manthiram, A. *J. Am. Chem. Soc.* **2013**, *135* (48), 18044–18047.